Proceedings of ASME Turbo Expo 2020
Turbomachinery Technical Conference and Exposition
GT2020
September 21-25, 2020, London, England

GT2020-15055

ENTROPY GENERATION AND EFFICIENCY OF A TRANSONIC ROTOR WITH WATER INJECTION - A NUMERICAL STUDY

Natan Zawadzki, Artur Szymanski,
David Alejandro Block Novelo, Uyioghosa Igie
Centre for Propulsion Engineering
School for Aerospace, Transport and Manufacturing
Cranfield University
Cranfield, Bedfordshire MK43 0AL
United Kingdom
Email: n.zawadzki@cranfield.ac.uk

ABSTRACT

The application of compressor water injection in aero-engines is of renewed interest in the civil aviation industry. Water due to its unprecedented heat capacity has the potential to cool the engine air through evaporation and thus reduce the NO_x emissions formed in a combustion process. It is well known that the evaporative cooling increases thermodynamic cycle efficiency and thus improves the fuel economy. A relatively unexplored area, however, is the entropy generation due to water phase change as well as the balance between the corresponding entropy yield and the savings from the cooling of the core compressor flow. Hence, little consensus in the literature exists on the ultimate effect of water injection on compressor efficiency. In this study, a numerical analysis of water injection on an axial transonic rotor was carried out. The compressor model was tested at near-peak efficiency conditions with and without water injection. The flow was analysed using the Eulerian-Lagrangian approach with two-way coupling and the k-ω Shear Stress Transport turbulence model with Reattachment Modification. A universal, second thermodynamic law approach to quantify the entropy generation is proposed and used to evaluate the compressor flow. Results show that evaporation can facilitate the compression process and does not impair the compressor efficiency if applied at favourable conditions. The entropy generation in droplet-laden flow scales according to the gains from cooling effect and losses due to the evaporation and increased friction in the fluid. Some of the discrepancies in the public domain could be addressed, showing that the observed improvement in compressor efficiency is highly sensitive to the entropy flux measurement location. Most benefits from water injection were observed at the rotor tip proving the case for part-span injection from an entropy balance perspective.

Keywords: *water injection, wet compression, entropy, efficiency, aerodynamic performance, axial compressor*

NOMENCLATURE

Latin Letters

AR	Aspect ratio, $-$
C	Root axial chord, cm
c_p	Specific heat at constant pressure, $J/kg/K$
c_v	Specific heat at constant volume, $J/kg/K$
d	Droplet diameter, $micron$
e	Internal energy, J/kg
ER	Expansion ratio, $-$
v	Specific volume, m^3/kg
f	Water mass fraction, $-$
f_n	Numerical factor, $-$
h	Specific enthalpy, J/kg
k	Heat transfer coefficient, $W/m/K$
L	Latent heat of evaporation, J/kg
$\dot{m}$	Mass flow, kg/s
M	Molar mass, kg/mol
N	Rotational speed, rpm
P	Pressure, Pa
R	Gas constant, $J/kg/K$
$\dot{S}_{gen}, \dot{s}$	Entropy generation, specific entropy flux, W/K
s	Specific entropy, $J/kg/K$

S_{ij}	Shear strain rate tensor
T	Temperature, K
$\mathbf{u}, u_i, u_j$	Velocity vector, m/s
u, v, w	Cartesian velocity components, m/s
x_i, x_j	Spatial vector
w	Vapour mass fraction, $-$
w_s	Specific work, $J/kg/K$
x, y, z	Cartesian coordinates
y^+	Dimensionless wall distance, $-$

Greek Letters

δ_{ij}	Kronecker delta
η	Compressor efficiency, $-$
ε	Rosin-Rammler exponent
μ	Dynamic viscosity, $Pa \cdot s$
∇	Nabla operator
ϕ	Viscous dissipation function, J/K
ρ	Density, kg/m^3
σ	Surface tension, N/m
τ	Wall stress, Pa
ζ	Number of grid nodes, $-$

Superscripts

a	Air
ev	Evaporation
$heat$	Heat conduction
g	Gas mixture
l	Liquid
v	Vapour
$visc$	Viscous
$'$	Isentropic

Subscripts

0	Total/stagnation parameter
1	Station 1 (rotor inlet)
2	Station 2 (rotor outlet)
ad	adiabatic
c	Compressor
eff	Effective
in	Domain inlet
mp	Melting point
out	Domain outlet
r, θ, z	Cylindrical components

INTRODUCTION

The civil aviation market grows at a faster pace than ever before [1]. At the same time, the industry is experiencing unprecedented pressure to reduce its environmental impact. The pursuit of enhancing cycle efficiency has made aircraft engines to burn fuel at higher pressures and thus higher temperatures, facilitating the formation of thermal NO_x. To enforce technological changes, the regulatory authorities have set ambitious targets towards NO_x reductions in the upcoming decades (ICAO - International Civil Aviation Organization: -60% in 2026 vs 2004 [1], ACARE - Advisory Council for Aeronautics Research in Europe: -90% in 2050 vs 2000 [2]). Compressor water injection (WI) is a measure which can reduce NO_x emissions in magnitude equal to or higher than state-of-the-art combustors. However, the ultra-low NO_x combustor technology takes many years to be developed, and in cases, the size and weight restrict their use to land-based gas turbines [3]. Historically, WI was a thrust augmentation tool used in military and some of the first passenger aircraft. The improvement in engine efficiency and hence specific power made this obsolete. Previous efforts to implement it as a NO_x reducing technology have failed due to increased system complexity and maintenance issues [4]. Emerging technologies like additive manufacturing, better maintenance procedures and the increased pressure to improve airports local air quality can make WI an attractive option towards tackling NO_x. WI can reduce the compressor delivery temperature (CDT) in up to 100°C [4,5] through evaporative cooling, thereby considerably limiting the formation of Nitrogen Oxides. Furthermore, recent research suggests that the payload may not be a limitation since the increase in thermal efficiency can outweigh the fuel penalties due to the extra weight [3]. This increase in efficiency is part of the core matters studied in the present paper.

A thorough experimental investigation of water injection in an aero-engine compressor is limited by the accessibility of the machine and challenges associated with measurements in rotating machinery. Those arise from intricate flow patterns and limited space for test equipment. Since its first introduction, compressor water injection was analysed with the aid of analytical and simplified numerical models [6]. Computational fluid dynamics (CFD) studies investigating axial compressor performance with water injection start emerging in the late 2000s. Szabo & Turner [7, 8] analysed the three-dimensional flow field in the NASA Rotor 37. The authors discussed a wide range of effects of water injection on transonic compressors at design and off-design conditions. They found that the compressor efficiency noticeably reduces with water injection.

The Rotor 37 was further utilised in more recent studies by Sun et al. [9] and Zhang et al. [10]. The studies showed that if water film is modelled at the compressor walls, the gain in efficiency and pressure ratio (PR) due to water injection is smaller than in cases where the film formation was neglected. Kofar-Bai et al. [11] and Liu et al. [12], analysed the NASA Stage 35, covering a wide range of effects on compressor performance as a function of droplet diameter and water-to-air ratio. Among others, they found that the turbulence kinetic energy (TKE) increases in the rotor region during wet operation. The stage efficiency was reported to decrease for most of the cases [11], with the exception of tiny droplet sizes (1 micron) and low injection rates (0.5-1%).

Khan & Wang [13, 14], and Bugarin et al. [15] analysed independently a single-stage axial compressor model by Hus and Wo [16] at design conditions, using 2D and 3D analysis. The focus in Ref. [13–15] was on the effects of inlet fogging on industrial gas turbine operation and erosion. Khan & Wang concluded in Ref. [13] that the pressure ratio rises due to wet compression, while in Ref. [14] the opposite is reported. However, in both investigations, an increased axial flow velocity is observed due to higher mass flow. According to Bugarin et al. [15], in turn, the results for PR differ depending on ambient temperature and air saturation.

Wang et al. [17] used a notional compressor cascade to analyse the effects of the injection position and found that a well-placed injection can be used to re-energise low energy fluid at the end walls and therefore reduce the losses.

A series of papers on water injection effects on cruise operation of a small single-spool turbojet engine was published by Sun et al. [18, 19] and Kofar-Bai et al. [11]. The primary interest of the authors was the potential reduction in NO_x emissions due to wet operation. The numerical results showed an improved pressure ratio and compressor efficiency for this engine.

Finally, Luo et al. [20] studied a large compressor with eight stages. The work looked into the detailed aspects of wet operation at nominal and near-stall conditions. From a comparison of a wide range of injection scenarios, it was concluded that wet compression could alleviate flow separation, and improve the flow capacity, pressure ratio and efficiency.

The review of the current CFD work shows frequent contradictions between the studies regarding the effects of WI on compressor performance. In practice, the efficiency of a compressor during water injection depends on multiple parameters. Examples include a variety of interactions between droplets and the carrier fluid, such as momentum, mass and heat exchange. They take place in different flow regions: in boundary layers, across shock waves, and in the wake mixing region. Further influencing parameters include wall impingement, vapour condensation and film creation, and the interactions between the particles. So far, little consensus exists as what is the overall effect of these factors on the compressor efficiency. Various approaches have been proposed as how to measure wet compression efficiency. Zheng et al. [21] distinguished between an equivalent adiabatic efficiency, wet isentropic compression efficiency and efficiency of wet compression. White & Meacock [22] defined an equivalent wet polytropic efficiency as a function of specific entropy increase across the compressor. However, both of these studies are based on analytical calculations that provide limited insight into the flow details.

Denton [23], states that the appropriate measure of loss in an adiabatic machine is entropy generation. As a process variable, entropy does not distinguish between the individual flow features and can be balanced for any flow volume of a thermodynamic system. Therefore, an entropy-based definition of compressor efficiency is more applicable to both dry and droplet-laden flows. Except for the study by Szabo & Turner [8], none of the CFD work accounts for the entropy generated due to the water phase change. However, the authors assume a tiny droplet size of 1 micron, which is rather of theoretical interest based on the current state-of-the-art atomisation technology.

This study focuses on the entropy generation mechanisms inside the compressor domain with and without water injection in an attempt to clarify some of the uncertainties related to wet compression efficiency. For the first time, the individual entropy generation sources of entropy generation related to thermodynamic processes within a compressor with water injection are quantified.

METHODOLOGY

Compressor Model

The NASA Rotor 67 (R67) was used in this study, and the geometry was rebuilt from the source design data in [24]. The design point (DP) parameters are summarised in Tab. 1.

The numerical domain comprises of a single blade passage divided into inlet, rotor and outlet duct. To reduce the influence of the inlet and outlet boundary conditions on the flow solution in the blade passage, the inlet and outlet ducts were stretched by 1.7 and 2.7 chord, respectively (see Fig.1). The compressor

Tab. 1 R67 design point parameters [24]

Rotational speed	N	*rpm*	16043
Mass flow	$\dot{m}$	*kg/s*	33.25
Pressure ratio	P_{02}/P_{01}	-	1.630
Adiabatic efficiency	η_{ad}	-	0.908
Blade count		-	22
Aspect ratio (avg.)		-	1.56
Tip radius		*cm*	25.70
Hub radius (inlet)		*cm*	9.64
Blade height		*cm*	16.06
Root axial chord	C	*cm*	9.03
Max tip speed		*m/s*	429
Tip relative Mach number		-	1.38

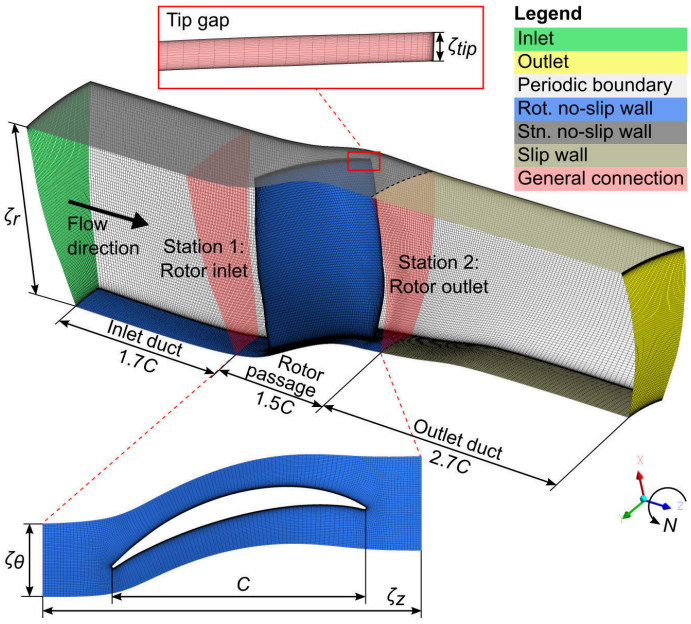

Grid properties

y^+	ζ_r tip	ζ_r	ζ_θ	ζ_z	ζ_z duct	ζ glob.	ER glob.	ER tip	AR max
2	39	144	48	124	90	4.0e6	1.2	1.2	1619

Fig. 1 R67 numerical domain and grid

model includes a constant height tip clearance of 1.016 *mm*. The hub clearances between the blade platform and adjacent inlet and outlet passages were not modelled.

Numerical Software

A commercial CFD software by ANSYS was used to complete the flow field analysis. TurboGrid was deployed for grid generation and CFX-Solver to solve the flow equations. CFX is a coupled, implicit and pressure-based Navier-Stokes solver. It utilises the vertex-centred finite-volume second order discretisation method for unstructured multiple elements.

Numerical Grid

The grid convergence study followed the Roache's guidelines [25]. A fine mesh with 4.0*e*6 nodes was selected. The first node was placed in the viscous sub-layer so that the area-averaged dimensionless wall distance y^+ was lower than two at all wall boundaries. All grid properties are summarised in Fig. 1.

Multiphase Flow Model

The analysis of both phases is performed using a steady-state Reynolds-Averaged Navier-Stokes (RANS) analysis in conjunction with the Shear Stress Transport Reattachment Modification (SST-RM) turbulence model. The k-ω SST-RM exhibits improved accuracy in compressor flow simulations [26–28]. The multiphase solution is obtained using the Eulerian-Lagrangian approach. For heat transfer, the energy equation is solved. Second-order advection and turbulence schemes are selected with conservative length scale control. The flow is solved in a rotating frame of reference, with the interfaces between meshes treated as a general connection. The flow composition is defined based on three materials: dry air, liquid water, water vapour, and their respective combinations: air- vapour and liquid-vapour mixture. The material properties are summarised in Tab. 2

Continuous phase: The gas is treated as a compressible mixture of air and vapour, and the properties are selected as listed in Tab. 2. In reality, all gas properties vary with temperature and pressure. However, for the expected range of flow conditions in the selected test case, the effect is negligible. The gas mixture is set to constraint, and the water vapour component is modelled via a transport equation.

Dispersed phase: The water is modelled as a spray of incompressible Lagrangian particles with two-way coupling between the phases. The liquid physical properties are listed in Tab. 2. Since water is nearly incompressible, the temperature and pressure dependence is weaker than in gases and thus the error due to the constant properties less significant. The drag force is calculated using the Schiller-Naumann correlation [29]. Collisions are modelled through Sommerfeld collision model [30] with the coefficients of restitution set to unity. The static and kinetic friction coefficients are neglected. Although in reality, the droplet impact is not fully elastic, small droplets are known to follow well the flow path and only sporadic collisions are expected, and thus a small error. Some studies ignore the droplet interaction completely [7, 8]. Droplet merging is not modelled. The particle breakup is modelled using a cascade atomization and breakup model (CAB) model [31] in conjunction with the Liu dynamic drag modification [32]. Wall condensation is not considered in this study.

Tab. 2 Material properties

		Air	H_2O vapour	H_2O liquid
State		ideal gas	ideal gas	liquid
M	*kg/mol*	28.96	18.02	18.02
ρ	kg/m^3	from ideal gas	from ideal gas	958.37
c_p	*J/kg/K*	1006.6	NASA format	4215.6
k	*W/m/K*	0.026	0.679	0.019
μ	*Pa·s*	Sutherland	2.8e-4	9.4e-6
σ	*N/m*	-	-	0.072

Tab. 3 Boundary conditions

Inlet		
Rotation		Stationary
Total pressure	$P_{0,in}$	101.325 *kPa*
Total temperature	$T_{0,in}$	288.15 *K*
Flow direction		axial
Turbulence intensity		5%
Vapour mass fraction	w_{in}	0%
Water mass fraction	f_{in}	2%
Droplet diameter	d^l_{in}	10 micron
Droplet size distribution		RR: $\varepsilon = 2.0$
Droplet spatial distribution		Uniform, equally spaced
Parcel number		100*k*
Injection velocity	v^l_{in}	30 *m/s*
Outlet		
Avg. static pressure		115 *kPa*
Static pressure profile blend		5%
Walls		Smooth, adiabatic

Between phases: The transitions of liquid water and its vapour is treated as a homogeneous binary mixture. The phase change is modelled based on vapour pressure determined from the Antoine equation. The heat and mass transfer during evaporation is captured using a built-in liquid evaporation model. The heat transfer between the gas mixture and the droplets is modelled via the Ranz-Marshall correlation [33].

Boundary Conditions

The boundary conditions are summarised in Tab. 3. The dry rotor performance is tested at near-peak efficiency at inlet Sea-Level Static (SLS), International Standard Atmosphere (ISA) day conditions. In R67, the near-peak efficiency NPE is slightly different from the design point (DP) conditions (see Fig. 1), which is positioned closer toward surge, at a slightly

higher PR. A medium turbulence intensity of 5% is assumed at the inlet. The wall motion and type is indicated in Fig. 1. The outlet duct hub and shroud are slip walls to eliminate the upstream effect of the boundary layer growth. The back static pressure was kept the same ($115kPa$) for both dry and wet operation, and it was allowed to vary within 5% of the specified value.

Water is introduced at the inlet of the R67 domain. The injection is discrete, i.e. no nozzles are modelled. The number of droplets that would be typically present in a spray injection is characterised by so-called parcels which are a statistical representation of particles that share the same characteristics. A $100k$ parcels were found to represents a converged solution and were imposed at a uniform particle mass flux, constant liquid temperature and fixed water-to-air ratio of 2% (based on the dry inlet air mass flow). The 2% was selected as a compromise between maximising the effects of the evaporation and staying within safe limits as 3% were reported as the maximum water content for a stable compressor operation [34]). The particle diameter is assigned according to Rosin-Rammler (RR) distribution with the exponent set to 2.0, which is considered typical for atomised liquid [35]. A full rebound of droplets is modelled at the walls, and therefore no wall-film model is utilised. Since small particles follow well the main flow path, they are unlikely to impinge on the walls.

Entropy Generation

The methodology proposed by Szabo & Turner [8] was selected as a basis for wet compressor efficiency considerations. It relies on a discrete calculation of three sources of irreversible losses in the post-processing phase: viscous dissipation, conductive heat transfer and energy exchange between phases. For grids with low wall resolution, the approach made use of wall functions to model the viscous entropy generation. The overall entropy gain was obtained by summing up and integrating the local entropy production terms across the entire flow volume.

Since the grid used in this study resolves the boundary layer at all walls down to $y^+ = 2$, it was attempted to integrate the viscous dissipation without deploying any wall treatment. A test on a dry flow solution showed that despite the fine wall resolution, the viscous entropy generation in the boundary layer was massively underestimated (by a factor of two). An implementation of an adequate wall treatment turned out very challenging due to the limited modifiability of commercial software. Therefore, adjustments in the approach were necessary. To obtain an estimate of the total entropy generation, a more straightforward and universal approach was used instead based on the balance of specific entropy fluxes at two arbitrary locations. The entropy generation between inlet and outlet of a compressor was defined as follows:

$$\dot{S}_{gen} = \dot{m}^a \left\{ (1+w_2-w_1)\left[c_p^g ln\left(\frac{T_{02}^g}{T_{01}^g}\right) - R^g ln\left(\frac{P_{02}^g}{P_{01}^g}\right)\right] + c_p^l \left[f_2 ln\left(\frac{T_{02}^l}{T_{mp}^l}\right) - f_1 ln\left(\frac{T_{01}^l}{T_{mp}^l}\right)\right] + w_2\frac{L_2}{T_{02}^g} - w_1\frac{L_1}{T_{01}^g} \right\} \quad (1)$$

A detailed derivation of the Eqn. 1 is presented in Appendix A.

Despite the underestimated results when integrated without wall modelling, the formulation of viscous entropy generation used in Ref. [8] provides a valuable source of localised information on a major loss mechanism (friction) in the compressor outside of the inner boundary layer ($y^+ > 35$). The definition of the viscous entropy generation was first introduced by Bejan [36] so that:

$$\dot{S}_{gen}^{visc} = \frac{\phi}{T} \quad (2)$$

Where ϕ is the viscous dissipation function and T the static fluid temperature. For RANS solution of turbulent flows, Bejan [36] approximated the fluctuating part of ϕ using the effective viscosity concept:

$$\phi = \mu_{eff}\left[2\left(\frac{\partial u}{\partial x}\right)^2 + 2\left(\frac{\partial v}{\partial y}\right)^2 + 2\left(\frac{\partial w}{\partial z}\right)^2 + \left(\frac{\partial v}{\partial x}+\frac{\partial u}{\partial y}\right)^2 + \left(\frac{\partial w}{\partial y}+\frac{\partial v}{\partial z}\right)^2 + \left(\frac{\partial u}{\partial z}+\frac{\partial w}{\partial x}\right)^2 - \frac{2}{3}(\nabla\cdot\mathbf{u})^2\right] \quad (3)$$

From Eq. 3, it can be seen that the viscous dissipation depends exponentially on the velocity gradients. Regions of very steep gradients as in boundary layers rely on extremely fine mesh resolution. Even though the fine boundary layer mesh of $y^+ < 2$ produced an acceptable velocity profile at the wall, the uncertainty in the entropy production is quadratic.

The second entropy source in the discrete formulation according to Ref. [8] is the conductive heat transfer between the fluid elements. Following a similar logic as for the viscous dissipation function, the Reynolds-averaged entropy generation due to heat conduction is:

$$\dot{S}_{gen}^{heat} = \frac{k_{eff}}{T^2}(\nabla T)^2 \quad (4)$$

Since the effective thermal conductivity k_{eff} is neither included in Ref. [8] nor calculated by the solver, the authors propose to approximate it based on kinetic gas theory (see Appendix B).

The aforementioned entropy generation mechanisms due to fluid friction and heat exchange occur in both phases. The last source of entropy generation is the heat and mass transfer between the carrier flow and the particles. Since it is very challenging to capture it without enhanced access to the advanced particle properties, it is not analysed in this study.

Compressor Efficiency.

The compression efficiency is understood as a ratio of isentropic to real compression work. It can be further modified to be a ratio of entropy generated in the domain to the enthalpy flux across the system boundaries:

$$\eta_c = 1 - \frac{T_{02}\dot{S}_{gen}}{\dot{m}^a\left[c_p^g(T_{02}^g - T_{01}^g + w_2T_{02}^g - w_1T_{01}^g) + c_p^l(f_2T_{02}^l - f_1T_{01}^l)\right]} \quad (5)$$

A detailed derivation of Eqn. 5 is presented in Appendix A. The Eqn. 1 to 5 were implemented in CFX in post-processing phase using CEL language and used for the evaluation in this study.

Metrics

To quantify the effect of water injection on overall entropy production in the compressor, the entropy flux balance and compressor efficiency were calculated for each part of the numerical domain: inlet duct, rotor passage and the outlet duct. To gain more insight into the loss generation mechanism, each term of the Eqn. 1 was evaluated individually. Moreover, the local entropy generation due to friction and heat conduction was examined at different span-wise positions in the flow based on Eqn. 3 and 4. Additionally, to the entropy analysis, the changes in the compressor flow were evaluated in terms of:

- One-dimensional mass flow averaged parameters (both in the circumferential and radial direction): total mass flow, rotor PR, rotor TR, total pressure and temperature, water and vapour mass fraction; area-averaged wall stress.
- Two-dimensional span-wise profiles (circumferentially mass flow averaged): total and static temperature and pressure, Mach number, gas density, axial flow velocity, turbulence kinetic energy (TKE), average mean particle diameter (MPD), particle number density (PND), averaged particle velocity, vapour mass fraction w, and the viscous and conductive entropy generation.

The 1D averages and 2D radial profiles were evaluated at the inlet, and at the following downstream stations: rotor entry (Station 1), rotor exit (Station 2), outlet (see Fig. 1).

RESULTS & DISCUSSION

The radial flow distribution for the dry and wet case are presented in Fig. 2 and 3 along with the dry test data from [24]. A characteristic feature of virtually all two-equation RANS closure models is the underpredicted pressure in the tip region [37] and consequently lower gas density. The discrepancy between the CFD and the experiment may appear visually large due to the scaling of the axis which was selected to show the difference between the wet and dry flow solution. Nevertheless, the numerical predictions match well the test data, and the overall accuracy is satisfactory according to the current standards of a steady-state, single passage analysis.

The most distinctive feature of water injection, seen across all literature, is the drop in total temperature. In the presented test case, the reduction in rotor TR is relatively small (1%) owed to the low ambient temperature (ISA standard day conditions 288.15 K, 1 atm) and the fact that it includes only one rotor. The absolute reduction of total temperature at the rotor exit is 4.7 K and at the domain outlet almost 9 K. Approximately 4.6% of the water evaporates across the rotor passage. A similar amount is evaporated in the inlet domain (5.3%) and almost double the amount (8.7%) in the outlet duct. In total, only 18.2% of the injected water was evaporated, and the rest left the domain in a liquid state.

The total mass flow rises as expected but only by 1.8%, which is less than the water injection rate. If to subtract the 2% added by mass of water (part of which is evaporated so that $f+w=0.02$ applies everywhere in the domain), the net airflow

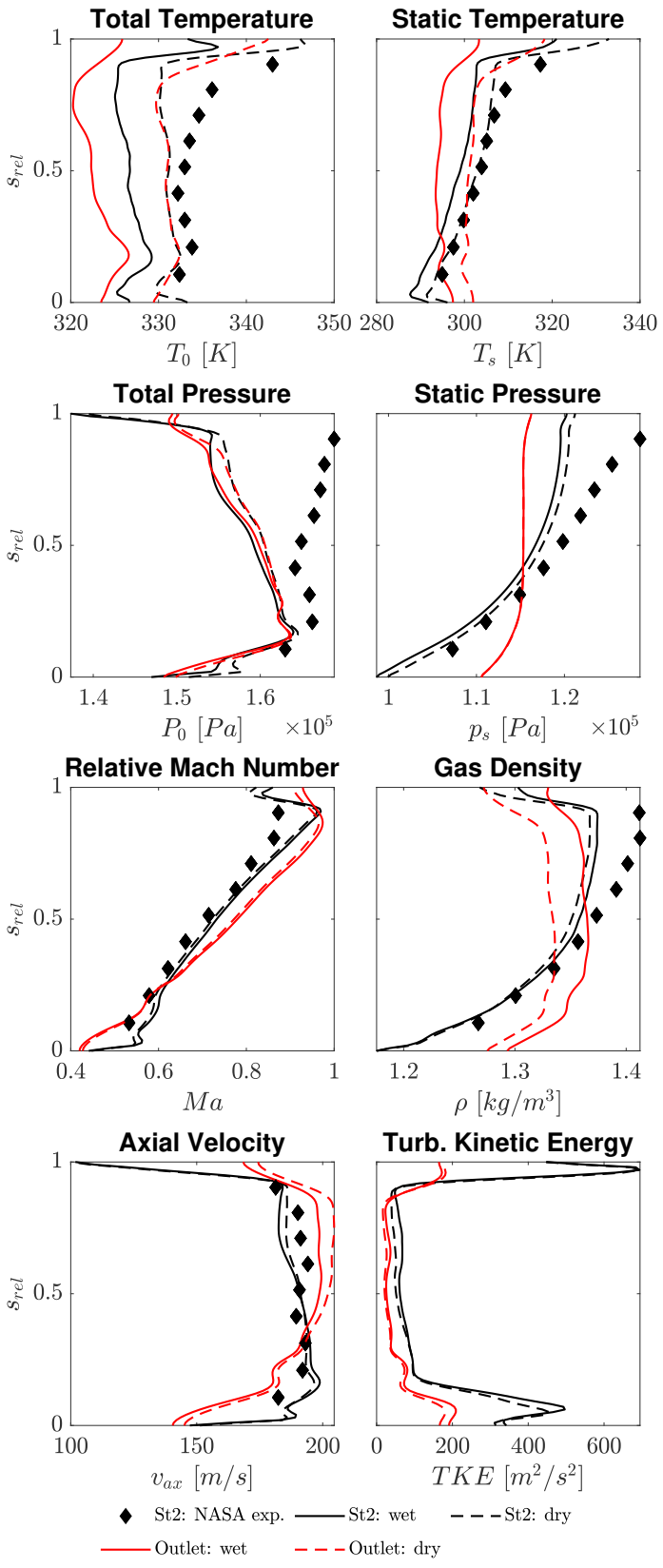

Fig. 2 Span-wise wet and dry flow distribution vs NASA experiment [24]. The total and static pressure, total temperature and velocity were measured. The remaining reference parameters are calculated from the experimental data using ideal gas equation and isentropic relations.

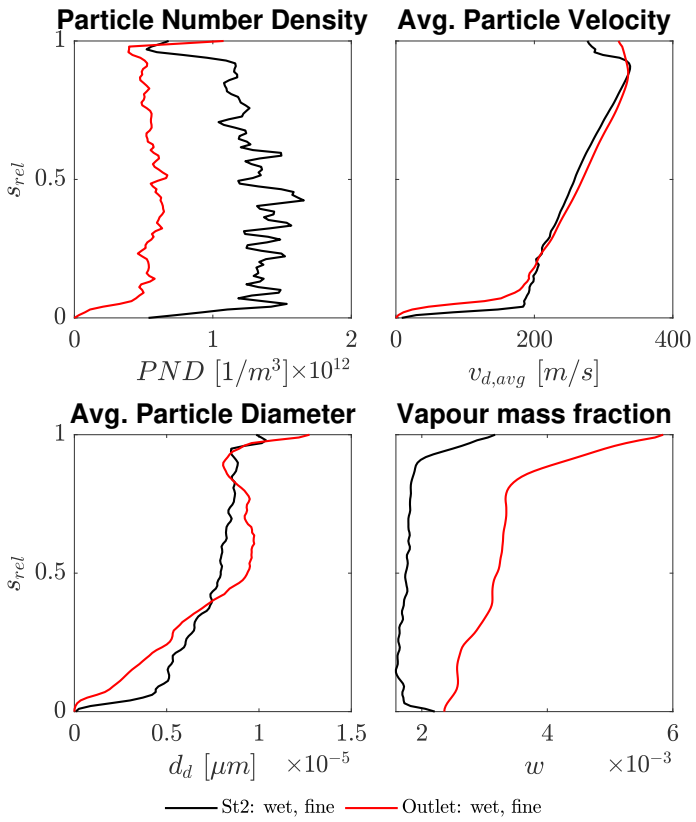

Fig. 3 Span-wise particle distribution and vapour mass fraction

is less than in the dry case. This partially contradicts previous studies since the air mass flow was commonly found to increase through the evaporative cooling beyond the additional mass of water. As the air becomes denser, theoretically more air can be accommodated by the same geometry at a fixed mechanical speed. In this case, the denser air is offset by a drop in axial velocity (see Fig. 2) so that effectively, the mass flow increase is not significant. Possible explanation relates to the back static pressure selection at the outlet, which was held constant both in dry and wet case. In practice, the pressure is a function of the irreversible upstream losses. Since both the stagnation pressure and static temperature were found to reduce during WI in this study, applying the same dry back static pressure for the wet case enforces a lower velocity. A small contribution to the velocity drop might also arise from momentum transfer between the phases since the droplets are injected at a considerably lower speed than the bulk flow (30 vs 170 m/s).

Overall Entropy Generation Results

A detailed breakdown of the entropy generation is presented in Tab. 5. In each part of the domain, the overall entropy production is broken down into the individual entropy sources as of Eq. 1: temperature rise/drop (TR), pressure rise/drop (PR), and evaporation. A minus sign indicates that entropy is "removed", i.e. the system gains order. The temperature change of droplets is neglected.

In a wet inlet duct, the entropy "savings" due to the cooling effect are not enough to offset the entropy generation due

Tab. 4 Dry vs wet compressor results

		Dry	Wet	Δ %
$\dot{m}$	kg/s	34.26	34.88	1.8
P_{02}/P_{01}	-	1.566	1.562	-0.3
T_{02}/T_{01}	-	1.151	1.139	-1.0
$P_{0,in}/P_{01}$	-	0.9986	0.9941	-0.4
$P_{0,out}/P_{02}$	-	0.9971	0.9998	0.3
$T_{0,out}$	K	331.8	327.0	-2.7
τ_w	Pa	174.59	183.76	5.3
f_{out}/f_{in}	%	-	18.15	-

to the phase change. Furthermore, since there is no compression, the increase of entropy generation from 0.62 to 2.64 W/K suggests a higher pressure loss when water is injected. Overall, from the entropy generation perspective, the inlet duct operates under less favourable conditions compared to a dry case. Higher temperature differences facilitate the heat exchange between the phases. If the compressor rotor would operate at higher ambient temperatures, the air cooling effect might outweigh the adverse entropy generation in the inlet duct, and therefore further enhance the mass flow. The discrepancy between the presented case and the literature may, therefore, arise from the fact that most of the studies were done on injection at elevated ambient temperature as historically, the primary interest of the industry was power restoration. This observation implies that there is a minimum temperature limit where no benefit from water injection is achieved.

A different situation occurs in the rotor, where the overall entropy generation is approximately half of that in the dry case. The evaporative cooling counteracts the temperature rise due to the irreversible losses across the rotor, resulting in almost 18 W/K entropy flux difference. The rise in fluid pressure reduces the system disorder, thus the entropy production is negative both for the dry and wet case. However, in the wet case, a slightly smaller amount of entropy is recovered, confirming that water injection contributes to the pressure loss. Overall, the cooling effect substantially outweighs the entropy generated due to the pressure loss and phase change. To determine whether the reduced entropy generation translates into more favourable rotor operation during WI, the enthalpy flux balance must be taken into the equation. Since the fluid is compressed across the rotor, the enthalpy rises both in the wet and dry case. However, a lower enthalpy rise in the wet case indicates less specific compression work. Along with the diminished entropy production, the compressor rotor experiences a 4.4 per cent point boost in the efficiency.

In the outlet duct, the entropy production depends again on balance between the higher pressure loss, evaporation, and the cooling effect. Since both the gas temperature behind the rotor and the residence time (due to the outlet duct dimensions) are higher than in the upstream sections, the heat exchange is facilitated. Consequently, more droplets evaporate, generating high

Tab. 5 Detailed breakdown of entropy generation, enthalpy and compressor efficiency

		Dry	Wet
Inlet Duct			
h_{in}	*kJ/kg/K*	289.4	314.6
$\dot{S}_{gen}$	*W/K*	0.67	9.91
TR	*W/K*	0.05	-5.59
PR	*W/K*	0.62	2.64
Evap.	*W/K*	0	12.87
Rotor Passage			
η_c	*%*	**90.2**	**94.6**
$h_2 - h_1$	*kJ/kg/K*	43.8	42.7
$\dot{S}_{gen}$	*W/K*	20.07	11.04
TR	*W/K*	220.76	203.20
PR	*W/K*	-200.69	-199.66
Evap.	*W/K*	0	7.13
Outlet Duct			
h_{out}	*kJ/kg/K*	333.4	349.5
$\dot{S}_{gen}$	*W/K*	1.91	-2.14
TR	*W/K*	0.61	-20.15
PR	*W/K*	1.30	0.10
Evap.	*W/K*	0	17.91
Total			
η_c	*%*	**89.0**	**88.8**
$h_{out} - h_{in}$	*kJ/kg/K*	43.9	34.9
$\dot{S}_{gen}$	*W/K*	22.65	18.82

amounts of entropy at a rate of 17.91 W/K. However, at the same time, the intensified evaporation enhances cooling. The "savings" from the temperature reduction outweigh the entropy gain due to the phase change, and the overall balance is negative, i.e. the outlet acts as an entropy sink.

The contrasting effects of water injection in the ducts versus the rotor passage lead to an interesting observation: if the wet efficiency is measured immediately at the rotor boundaries (between Stations 1 and 2, see Fig. 1), the compressor performance improves compared to dry case operation. On the contrary, if the whole passage length is considered and the efficiency is measured at the inlet and outlet of the domain, the compressor efficiency deteriorates and is slightly lower than in the dry case. In the first instance, the results may seem misleading, since the overall entropy generation in the entire domain is still lower than in a dry case (18.85 vs 22.65 W/K). However, it is the balance between the entropy generation and the enthalpy gain that determines whether the compressor operates at favourable conditions. During WI, more enthalpy is available at the domain inlet due to the higher internal energy of water compared to air. If the fluid is cooled down without simultaneous compression, the displacement work p/ρ is zero and the enthalpy reduces at the same rate as the temperature. Even though the overall entropy generation is lower, the simultaneous reduction of enthalpy in the inlet and outlet duct results in efficiency loss. Therefore, water injection is beneficial if the entropy is reduced at a faster rate than the enthalpy, which in this case happens only if positive displacement, i.e. compression work is done. This phenomenon might pose a challenge in multistage compressors, where the fluid passes through alternating compressor and stator (no compression) rows.

Local Flow Field Results

The overall entropy generation could not be obtained from integration of the local flow field in each domain due to the lack of adequate wall treatment. Therefore, a direct comparison with the 1D average is not possible. However, investigation of the viscous dissipation function and heat conduction in the flow provides additional insights on how water injection can locally facilitate or diminish the losses. The entropy generation due to the fluid friction is expected to be far more dominant than other sources of losses [8] and therefore, the primary attention is paid to the viscous dissipation.

In Fig. 4, the entropy generation per unit volume due to viscous dissipation ϕ/T and heat conduction is presented as a difference between the wet and dry case ($\Delta\dot{S}_{gen} = \dot{S}_{gen,wet} - \dot{S}_{gen,dry}$). The scale is clipped to smaller values than the maximum range to reveal the entropy production in the core which is an order of magnitude (or more) smaller than the losses in the inner boundary layer but occupies a significantly larger area.

The effect of water injection is distinctive in the blade tip region (99% span). Here, the entropy generation is greatly reduced compared to the dry case in the blade front and mid-chord region, occupied by a complex shock structure. Immediately behind the compression waves, an area of significantly higher losses is visible in the form of a red streak that originates from near the trailing edge at the suction side (SS). It stretches across the whole passage width to eventually collide with the pressure side (PS) of the consecutive blade and mix in into its wake. The region marks the trajectory of the tip leakage vortex (TLV) which intensifies when water is injected. The entropy yield is also noticeably higher in the wake mixing region illustrated as yellow trails smearing off the blade trailing edge.

A similar loss pattern occurs at 50-90% blade span: Under WI, the entropy production decreases across the shock waves, but intensifies just after, which is particularly visible downstream the normal passage shock. The shock waves are known to be weakened by droplets [38], and therefore less kinetic energy is dissipated by friction in these across the flow discontinuity. As opposed to the blade tip region, in the core flow, the separation and wake losses are the dominant source of entropy. This is made visible in Fig. 4 by clipping the range to two orders of magnitude lower value at 70 and 90% span. A distinctive feature of the blade wake pattern is the double streak suggesting that most of the losses happen at the outer parts of the wake region and the core is relatively unaffected by WI. At the hub, no shock is present, and the effect of water is visible mainly in regions of strong fluid ac- or deceleration, i.e. at the leading edge and

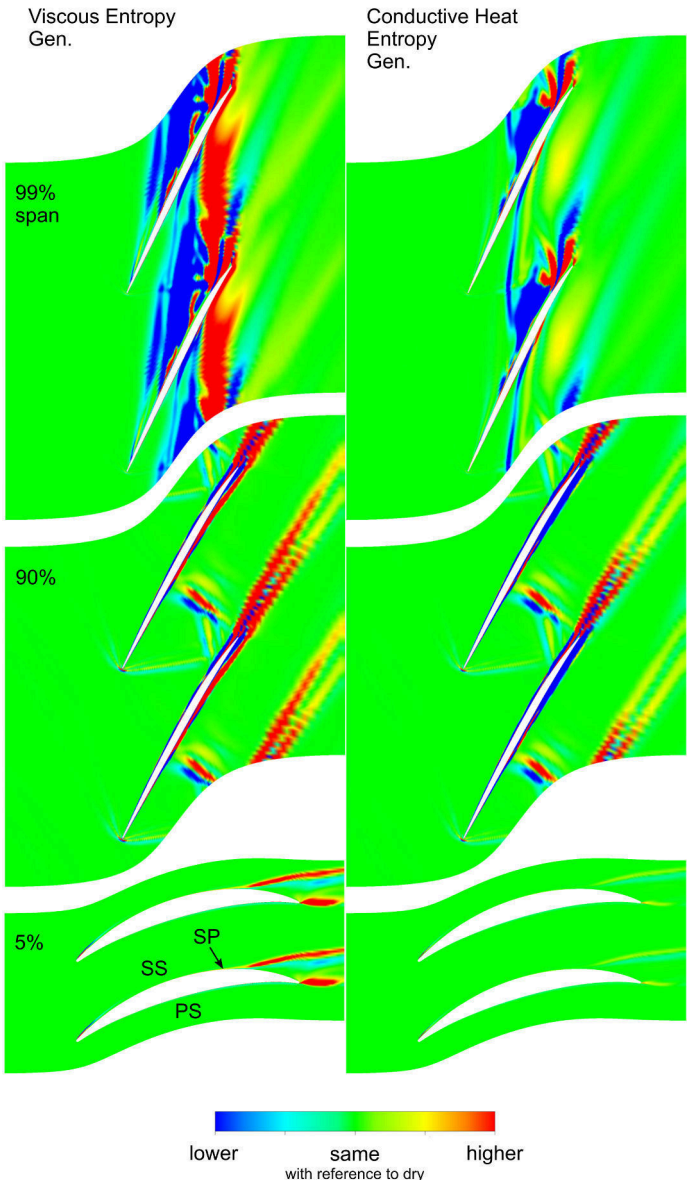

Scale bounds	$\dot{S}^{visc}_{gen}$ $W/m^3/K$		$\dot{S}^{heat}_{gen}$ $W/m^3/K$	
Span	Min	Max	Min	Max
5, 99%	-8.0e4	8.0e4	-4.0e4	4.0e4
90%	-8.0e2	8.0e2	-4.0e2	4.0e2

Fig. 4 Blade-to-blade difference (wet minus dry) of entropy generation per unit volume due to viscous dissipation (ϕ/T) and heat conduction

the point of flow separation (SP), both on the suction side of the blade. Based on these observations the most differences in entropy production between the dry and wet case occur either at the very tip or at the hub - areas where most losses are generated in a compressor regardless of water injection.

The determining of the underlying phenomena for the observed changes in the entropy generation is not straight-forward. Introducing water into the flow affects its dynamics by altering

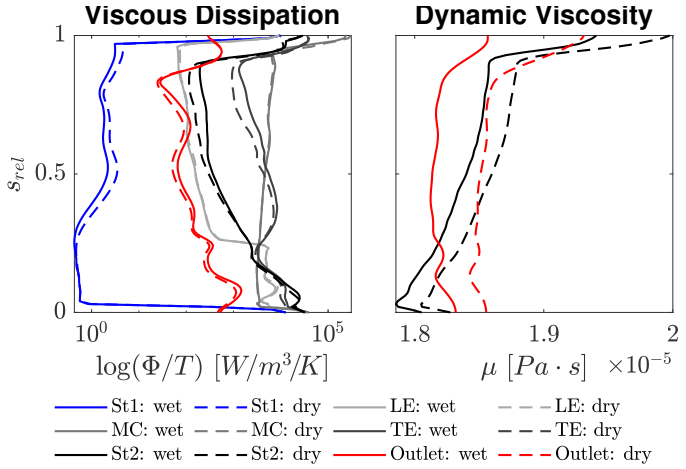

Fig. 5 Span-wise distribution of viscous entropy generation per unit volume at rotor inlet (St1), leading edge (LE), mid-chord (MC), trailing edge (TE) and rotor outlet (St2)

both the chemical and physical gas properties. The viscous dissipation is driven by the changes in fluid properties in terms of the dynamic and turbulent (eddy) viscosity and a set of complex terms involving velocity gradients. These refer to the different forms of fluid motion and deformation. Due to the direct link of these properties to the friction-induced entropy generation, it appears sensible to start the discussion investigating them individually.

The change in gas composition and temperature has a profound effect on the dynamic and turbulent viscosity, which in turn determine how the fluid deformation contributes to the friction and thus to the losses. The air viscosity is directly proportional to the fluid temperature and inversely to the vapour content (humidity). Both cooling and vapour release occurs during the evaporation. Therefore, in the areas of intensified heat exchange between the continuous and the liquid phase, the gas will experience less friction, assuming constant fluid deformation. Apart from the very tip, the influence on viscosity from increased vapour content is marginal in this case, and interestingly, the vapour mass fraction does not noticeably increase across the shock waves as shown in Fig. 7, despite a sudden temperature jump. A comparison of the plots of total temperature, dynamic viscosity and ϕ/T in Fig. 6 shows that the areas of intensified cooling and reduced viscosity match well with the regions of a lowered entropy generation. However, in other areas, e.g. alongside the tip leakage vortex trajectory at 99% span, or at the hub at the trailing edge of the blade, the changes cannot be explained solely by the altered dynamic viscosity.

In RANS the turbulent fluctuations of the flow are not resolved but averaged and modelled. Therefore, it is practical to express the turbulence contribution to the shear stress in terms of an artificial gas property - the turbulent viscosity. The effective viscosity is, therefore, a sum of the actual and turbulent viscosity component and it allows for a simplified characterisation of turbulent behaviour of a specific type of fluid. In Fig. 6, the effective viscosity μ_{eff} plot is juxtaposed with the turbulence kinetic energy (TKE). The relation between them is complex since, in

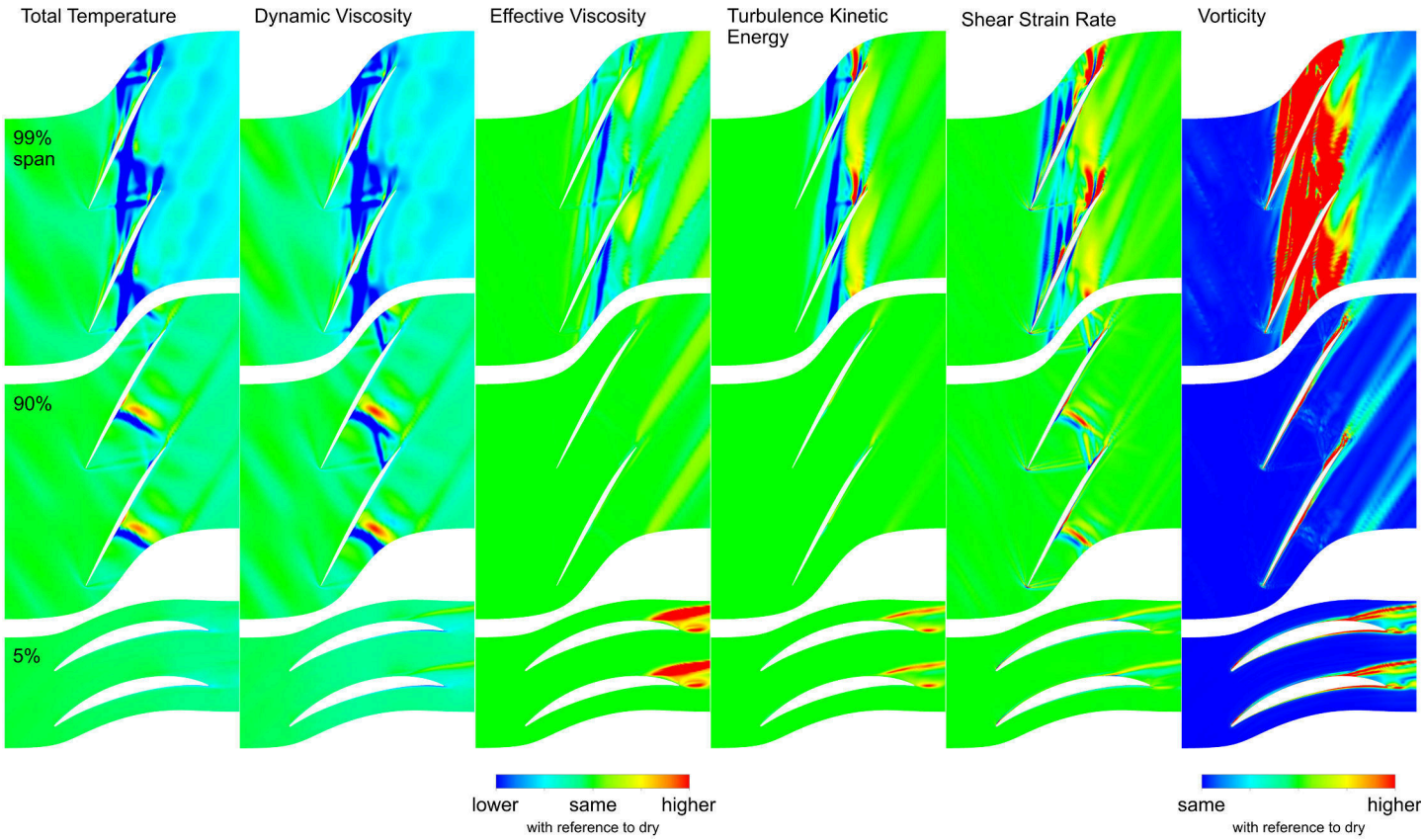

Scale bounds	T_0		μ		μ_{eff}		TKE		S_{ij}		$\nabla \times \mathbf{u}$	
	K		$Pa \cdot s$		$Pa \cdot s$		m^2/s^2		$1/s$		$1/s$	
Span	Min	Max	Min	Max	Min	Max	Min	Max	Min	Max	Min	Max
5, 90, 99%	-25.0	25.0	-1.0e-6	1.0e-6	-6.0e-3	6.0e-3	-1800.0	1800.0	-5.0e+4	5.0e+4	0.0	1.7e+4

Fig. 6 Blade-to-blade flow difference (wet minus dry)

the SST turbulence model, both parameters are functions of each other. However, the comparison of these two parameters brings about a conclusion that water injection energises the turbulent fluctuations in the flow, thus contributing to the entropy generation in the bespoken areas. The enhanced flow perturbation is particularly visible in the tip region across the TLV trajectory. Both the TKE and μ_{eff} charts also indicate an increased level of turbulence in the wake, especially near the hub at the outer boundaries of the hub corner vortex, forming two characteristic parallel streaks.

The viscous effects are also driven by the rate of fluid deformation in each direction. This can be shown by factoring out the velocity gradient in the Eqn. 3 so that:

$$\phi = 2\mu_{eff}\left[\frac{1}{2}\left(\frac{\partial u_i}{\partial x_j}+\frac{\partial u_j}{\partial x_i}\right)-\frac{1}{3}\left(\nabla\cdot\mathbf{u}\right)\delta_{ij}\right]\left(\frac{\partial u_i}{\partial x_j}\right) \quad (6)$$

Where $S_{ij} = \left(\frac{\partial u_i}{\partial x_j}+\frac{\partial u_j}{\partial x_i}\right)$ is the strain rate. The components of the strain tensor determine the stretching, compression and distortion of the fluid elements. While compression can increase the system order and is expected to counteract the expansion and distortion, the two latter parameters can be great contributors to the entropy generation. The strain rate at selected span-wise positions is also presented in Fig. 6. Not surprisingly, areas where the entropy increases with the presence of water, experience excessive strain.

It is also practical to look at the fluid vorticity $\nabla \times \mathbf{u}$, i.e. the spin of the fluid elements around their local axis, which is included in the last column of Fig. 6. The vorticity dramatically increases in the after-shock regions as well as in the separation and mixing zones. The familiar double-streak structure appears in the wake region, showing that the fluid rotation is excessive and drives the entropy generation. The propensity of the fluid to higher vorticity and turbulence is at first not apparent. However, recalling that the viscosity is reduced in the regions of intensified cooling, the flow perturbations are facilitated.

To summarise, apart from the very tip of the blade, there are only small regions where the entropy is decreased by water injection. The overall impression is that these entropy "savings" are not significant and cannot make up for the favourable en-

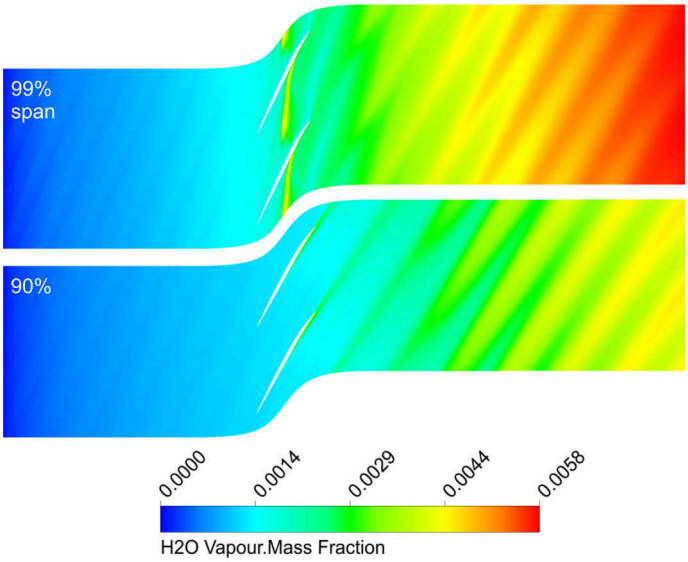

Fig. 7 Blade-to-blade plots of vapour mass fraction

tropy balance in the rotor during WI (see Tab. 5). These observations are easily verified in Fig. 5 where the radial distribution of the entropy generation due to viscous dissipation and conductive heat transfer is shown. In a wet case, the entropy gain is higher alongside almost the entire span inside the blade passage from the leading edge onwards. However, at the tip where the losses are up to two orders of magnitude higher than at midspan, the balance if favourable for wet operation. Interestingly, at the rotor inlet (Station 1) outside of the boundary layer, the ϕ/T is lower than in a dry case, implying that the observed higher pressure loss in Tab. 5 must solely arise from viscous wall effects. In Fig. 5 this is not visible due to the aforementioned lack of wall-treatment for entropy generation. The fact that WI may significantly contribute to the loss generation in the boundary layer, as seen by [8], underpins the case for part-span injection and avoiding the hub region. The root of a compressor blade usually exhibits lower TR compared to the tip, not allowing to utilise the benefit of WI fully.

Along with the weakened shock waves, the increased core friction explains the lower PR obtained with wet compression. Therefore, WI on subsonic compressors may compromise less the compression rate. Due to the high magnitude of losses at the tip, WI may still result in an overall saving which is suggested by the independently calculated 1D averages of entropy generation in the rotor in Tab. 5. If the entropy gain were confirmed utilising the discrete approach, it would be an argument for dedicated tip-only water injection for improved performance range and stall control.

Finally, the entropy generation due to the conductive heat transfer (see Fig. 4) exhibit a very similar behaviour to viscous entropy generation ϕ/T. In areas where the viscous dissipation is moderated by water injection, also less heat conduction happens. Regions of increased viscous dissipation result in more heat being transferred between the fluid layers and thus higher entropy generation due to heat conduction.

CONCLUSIONS

In this study, a universal approach to quantify entropy production and compressor efficiency in multiphase flows was proposed. The work presents a comprehensive examination of the entropy generation in an isolated, axial transonic compressor. Its implications on the compression efficiency were quantified on a reliable numerical framework for a practically implementable water injection scenario. The compressor model was NASA Rotor 67, and it was tested at near-peak efficiency operation, at standard day conditions, with 2% water-to-air ratio and 10 micron droplet diameter. The conclusions are as follows:

- The effect of water injection on the compressor losses strongly depends on the balance of two competing mechanisms: entropy reduction due to the evaporative cooling and entropy generation due to the droplet phase change.
- The performance benefit from water injection also depends on the initial gas temperature. In ducts, where only fluid transport but no compression occurs, the benefit of water injection can be seen only at elevated temperatures, as observed in the outlet duct. Besides icing concerns, this proves the point of injection behind the fan in a turbofan compressor, where the temperature is always higher than ambient.
- The rotor performance, is enhanced with water injection even at 288.15 K ambient air temperature since the cooling effect facilitates the compression process. The evaporative cooling has a two-fold effect: it slows down the temperature rise across the compressor due to the irreversibilities, and it reduces the required specific compression work.
- The overall efficiency improvement in any compressor component with water injection is determined by the corresponding balance of entropy and enthalpy gains. In compressors where the wet flow passes through long ducts with no compression, the enthalpy may reduce at a faster rate than the entropy is recovered due to the evaporative cooling, resulting in a lower entropy generation but also lower compressor efficiency.
- The wet compression efficiency is therefore sensitive both to the measurement and injection location. Extending the control or injection volume beyond the compression region can include passages that do not benefit from water injection and therefore, no improvement in compressor efficiency will be observed.
- A multistage compressor may further benefit from water injection as the number of “cold” ducts is reduced compared to the number of “hot” passages and rotor stages.

By evaluating the efficiency through entropy generation, this article shows that WI can improve compressor efficiency. However, the benefits rely on a careful selection of the injection region depending on the compressor inlet conditions.

REFERENCES

[1] ICAO, 2019. ICAO 2019 Environment Report. Tech. rep., International Civil aviation Organisation.

[2] ACARE, 2017. Strategic Research & Innovation Agenda. Tech. rep., Advisory Council for Aeronautics Research in Europe.

[3] Block Novelo, D. A., Igie, U., and Nalianda, D., 2019. "Onboard compressor water injection for civil aircraft emission reductions: Range performance with fuel burn analysis". *Transportation Research Part D: Transport and Environment,* ***67***, Feb, pp. 449–463.

[4] Daggett, D. L., 2004. Water Misting and Injection of Commercial Aircraft Engines to Reduce Airport NOx. Tech. rep., NASA/CR-2004-212957.

[5] Block Novelo, D. A., Igie, U., Prakash, V., and Szymański, A., 2019. "Experimental investigation of gas turbine compressor water injection for NOx emission reductions". *Energy,* ***176***, Jun, pp. 235–248.

[6] Murthy, S., Reese, B., Arcangeli, G. T., and Tsuchiya, T., 1978. Analysis of water ingestion effects in axial flow compressors. Tech. rep., Air Force Aero Propulsion Laboratory.

[7] Szabo, I., 2007. "A Numerical Study of Water Injection on Transonic Compressor Rotor Performance". Doctoral thesis, University of Cincinnati.

[8] Szabo, I., and Turner, M. G., 2008. "An entropy based evaluation of efficiency of a transonic compressor rotor with water injection". In Proceedings of the ASME Turbo Expo, Vol. 6, pp. 167–179. ASME Paper No. GT2008-50248.

[9] Sun, L., Zheng, Q., Luo, M., Li, Y., and Bhargava, R., 2011. "On the Behavior of Water Droplets When Moving Onto Blade Surface in a Wet Compression Transonic Compressor". *Journal of Engineering for Gas Turbines and Power,* ***133***(8), Aug, pp. 1–10.

[10] Zhang, H., Jiang, B., Luo, M., Liu, X., Fan, S., Yang, L., and Zheng, Q., 2015. "Investigation of water film formation on blade surfaces of a wet compression transonic compressor rotor". In Proceedings of the ASME Turbo Expo, Vol. 3, pp. 1–14. ASME Paper No. GT2015-43129.

[11] Kofar Bai, D. G., Zhang, H., Zheng, Q., and Abdu, S., 2017. "Flow Assessment on the Effects of Water Droplets on Rotor Region of Wet Compression". *Defect and Diffusion Forum,* ***374***, Apr, pp. 131–147.

[12] Liu, C., Li, X., Zhang, H., and Zheng, Q., 2017. "Heat and mass transfer characteristics of water droplets in wet compression process". In Proceedings of the ASME Turbo Expo, Vol. 3, pp. 1–14. ASME Paper No. GT2017-63516.

[13] Khan, J. R., and Wang, T., 2008. "Simulation of inlet fogging and wet-compression in a single stage compressor including erosion analysis". In Proceedings of the ASME Turbo Expo, Vol. 7, pp. 193–206. ASME Paper No. GT2008-50874.

[14] Khan, J. R., and Wang, T., 2010. "3D modeling for wet-compression in a single stage compressor including liquid particle erosion analysis". In Proceedings of the ASME Turbo Expo, Vol. 5, pp. 205–218. ASME Paper No. GT2010-23722.

[15] Bugarin, L., Badhan, A., and Mao, S., 2014. "Numerical investigation of impact of relative humidity condition on droplet accumulation and film cooling on compressor blades". In American Society of Mechanical Engineers, Fluids Engineering Division (Publication) FEDSM, Vol. 1A, pp. 1–9.

[16] Hsu, S. T., and Wo, A. M., 1998. "Reduction of Unsteady Blade Loading by Beneficial Use of Vortical and Potential Disturbances in an Axial Compressor With Rotor Clocking". *Journal of Turbomachinery,* ***120***(4), oct, pp. 705–713.

[17] Wang, J., Zheng, Q., Sun, L., and Luo, M., 2012. "The effective positions to inject water into the cascade of compressor". In Proceedings of the ASME Turbo Expo, Vol. 3, pp. 979–992. ASME Paper No. GT2012-69158.

[18] Sun, L., Zheng, Q., Li, Y., Luo, M., Wang, J., and Bhargava, R. K., 2012. "Numerical through flow simulation of a gas turbine engine with wet compression". In Proceedings of the ASME Turbo Expo, Vol. 3, pp. 925–937. ASME Paper No. GT2012-68846.

[19] Sun, L., Sun, T., Wang, Y., and Yang, W., 2016. "Numerical simulation of pollutant emission of a turbojet engine with water injection". In Proceedings of the ASME Turbo Expo, Vol. 1, pp. 1–9. ASME Paper No. GT2016-57074.

[20] Luo, M., Zheng, Q., Sun, L., Deng, Q., Li, S., Liu, C., and Bhargava, R. K., 2011. "The numerical simulation of inlet fogging effects on the stable range of a transonic compressor stage". In Proceedings of the ASME Turbo Expo, Vol. 4, pp. 609–630. ASME Paper No. GT2011-46124.

[21] Zheng, Q., Shao, Y., and Zhang, Y., 2006. "Numerical simulation of aerodynamic performances of wet compression compressor cascade". In Proceedings of the ASME Turbo Expo, Vol. 4, pp. 857–865. ASME Paper No. GT2006-91125.

[22] White, A. J., and Meacock, A. J., 2003. "An evaluation of the effects of water injection on compressor performance". In Proceedings of the ASME Turbo Expo, Vol. 3, pp. 181–189. ASME Paper No. GT2003-38237.

[23] Denton, J. D., 1993. "Loss mechanisms in turbomachines". *Journal of Turbomachinery,* ***115***(4), Oct, pp. 621–656.

[24] Strazisar, A. J., Wood, R., Hathaway, M. D., and Suder, K. L., 1989. Laser Anemometer Measurements in a Transonic Axial-Flow Fan Rotor. Tech. rep., NASA.

[25] Roache, P. J., 1994. "Perspective: A Method for Uniform Reporting of Grid Refinement Studies". *Journal of Fluids Engineering,* ***116***(3), Sep, pp. 405–413.

[26] Bourgeois, J. A., Martinuzzi, R. J., Savory, E., Zhang, C., and Roberts, D. A., 2011. "Assessment of Turbulence Model Predictions for an Aero-Engine Centrifugal Compressor". *Journal of Turbomachinery,* ***133***(1), Jan, pp. 1–15.

[27] Cornelius, C., Biesinger, T., Galpin, P., and Braune, A., 2013. "Experimental and Computational Analysis of a Multistage Axial Compressor Including Stall Prediction by Steady and Transient CFD Methods". *Journal of Turbomachinery,* ***136***(6), p. 061013.

[28] Liu, B., An, G., and Yu, X., 2015. "Assessment of curvature correction and reattachment modification into the shear stress transport model within the subsonic axial compressor

simulations". *Proceedings of the Institution of Mechanical Engineers, Part A: Journal of Power and Energy,* ***229***(8), pp. 910–927.
[29] Schiller, L., and Naumann, Z., 1933. "A drag coefficient correlation". *VDI Zeitung*(77), pp. 318–320.
[30] Sommerfeld, M., 1996. *Modellierung und numerische Berechnung von partikelbeladenen Strömungen mit Hilfe des Euler-Lagrange-Verfahrens*. Shaker Verlag Aachen.
[31] Tanner, F. X., 1997. "Liquid jet atomization and droplet breakup modeling of non-evaporating diesel fuel sprays". In SAE Technical Papers.
[32] Liu, A. B., Mather, D., and Reitz, R. D., 1993. "Modeling the effects of drop drag and breakup on fuel sprays". In SAE Technical Papers.
[33] Ranz, W., and Marshall, W., 1952. "Evaporation from drops - Part I". *Chemical Engineering Progress,* ***48***(3), pp. 141–146.
[34] Williams, J., 2008. "Further effects of water ingestion on axial flow compressors and aeroengines at part speed". In Proceedings of the ASME Turbo Expo.
[35] ANSYS, 2019. ANSYS CFX-Solver Modeling Guide.
[36] Bejan, A., 2013. *Convection Heat Transfer*, 4th ed. John Wiley & Sons, Inc.
[37] Dunham, J., 1998. CFD Validation for Propulsion System Components. Tech. rep.
[38] Chauvin, A., Jourdan, G., Daniel, E., Houas, L., and Tosello, R., 2011. "Experimental investigation of the propagation of a planar shock wave through a two-phase gas-liquid medium". *Physics of Fluids,* ***23***(11), Nov, p. 113301.

Appendix A: Derivation of Entropy-Based Efficiency

Consider an open thermodynamic system in equilibrium with a single inlet and outlet. The overall entropy generation can be obtained from the entropy flux balance:

$$\dot{S}_{gen} = \dot{s}_2 - \dot{s}_1 = \dot{m}(s_2 - s_1) \tag{7}$$

If a carrier gas (here air), a liquid (water), and its vapour are present in the system, the overall entropy flux at the corresponding streamwise position z can be defined as a sum of the entropy fluxes in each phase:

$$\dot{s}_z = \dot{m}^a_z s^a_z + \dot{m}^l_z s^l_z + \dot{m}^v_z s^v_z \tag{8}$$

Applying Eqn. (8) for inlet and outlet, substituting in Eqn. (7) and separating for each phase, one obtains:

$$\dot{S}^a_{gen} = \dot{m}^a(s^a_2 - s^a_1) \tag{9}$$

$$\dot{S}^l_{gen} = \dot{m}^l(s^l_2 - s^l_1) \tag{10}$$

$$\dot{S}^v_{gen} = \dot{m}^v(s^v_2 - s^v_1) \tag{11}$$

The total mass within the system must be preserved. The air does not undergo a phase change and therefore:

$$\dot{m}^a_2 = \dot{m}^a_1 = \dot{m}^a = const. \tag{12}$$

The liquid may evaporate, and therefore its mass will be reduced at the expense of its vapour:

$$\dot{m}^l_2 + \dot{m}^v_2 = \dot{m}^l_1 + \dot{m}^v_1 = const. \tag{13}$$

In the further derivation, it is practical to express the liquid and vapour mass as fractions of the air mass. Therefore, for water and water vapour, it follows:

$$f = \frac{\dot{m}^l}{\dot{m}^a}, \quad w = \frac{\dot{m}^l}{\dot{m}^a} \tag{14}$$

Substituting Eqn. (14) into Eqn. (10) and (11), respectively, results in:

$$\dot{S}^l_{gen} = \dot{m}^a(f_2 s^l_2 - f_1 s^l_1) \tag{15}$$

$$\dot{S}^v_{gen} = \dot{m}^a(w_2 s^v_2 - w_1 s^v_1) \tag{16}$$

Now, one needs to determine how to describe the specific entropy change in the individual phases. Combining the first and second law for reversible thermodynamic processes results in the general form of the fundamental thermodynamic relation (Gibb's equation):

$$de = Tds - Pdv \tag{17}$$

Liquids are nearly incompressible fluids. For most relevant processes, the compressibility effects are entirely negligible. Therefore, one can assume that the volume occupied by the liquid phase stays the same ($dv = 0$). Substituting for $c_v T$ for the internal energy e in Eqn. (17) and rearranging for the entropy s it follows:

$$ds = c_v \frac{dT}{T} \tag{18}$$

The entropy of fluid is considered to approach zero when it solidifies. Therefore, the absolute entropy of a liquid at any streamwise location z in the domain can be expressed by integrating Eqn. (18) with reference to the substance melting point mp:

$$s_z - s_0 = c_v ln\left(\frac{T_{0z}}{T_{mp}}\right) \tag{19}$$

Substituting Eqn. (19) into (15) for inlet and outlet, it follows:

$$\dot{S}^l_{gen} = \dot{m}^a c^l_v \left[f_2 ln\left(\frac{T^l_{02}}{T^l_{mp}}\right) - f_1 ln\left(\frac{T^l_{01}}{T^l_{mp}}\right)\right] \tag{20}$$

If the droplet temperature remains unchanged $T^l_{02} = T^l_{01} = T^{in}_l = const$, the above expression simplifies to:

$$\dot{S}^l_{gen} = \dot{m}^a c^l_v (f_2 - f_1)\, ln\left(\frac{T^l_{in}}{T^l_{mp}}\right) \tag{21}$$

If the water fully evaporates in the compressor duct before reaching the outlet ($f_2 = 0$), the entropy generation $\dot{S}^l_{gen}$ equals to the negative of the initial entropy of liquid at the injection. The entropy initially "carried" by the liquid needs to be subtracted from the process as it transforms to a different phase and is now associated with its vapour. For gases which are compressible, often it is more practical to consider the thermodynamic changes in terms of pressure, temperature and density instead of the specific volume. Substituting $\rho = \frac{1}{v}$ and $h = e + \frac{p}{\rho}$ in Eqn. (17), it follows:

$$dh - \frac{P}{d\rho} - \frac{dP}{\rho} = Tds - \frac{P}{d\rho} \tag{22}$$

Knowing also that $h = c_p T$, we obtain from Eqn. (21) an alternative form of the Gibbs equation:

$$ds = c_p \frac{dT}{T} - \frac{dp}{\rho} \tag{23}$$

The integral form of Eqn. (18) depends on the assumptions on the specific heat and density. For most fluids, the c_p and ρ are functions of both temperature and pressure, although the dependence varies for different substances. For air, the specific heat at constant pressure is only a weak function of temperature and for the range of pressure and temperature expected in an isolated rotor are negligible. Assuming an ideal gas with $\rho = \frac{p}{RT}$ and constant c_p, and integrating Eqn. (23), for Eqn. (9) one obtains:

$$\dot{S}^a_{gen} = \dot{m}^a \left[c^a_p ln \left(\frac{T^a_{02}}{T^a_{01}} \right) - R^a ln \left(\frac{P^a_{02}}{P^a_{01}} \right) \right] \tag{24}$$

Term 1 on RHS refers to the entropy change due to the balance of irreversible losses and evaporative cooling. The entropy increases if the losses outweigh the cooling effect so that TR $>$ 1. Term 2 refers to the entropy change due to the gain in total pressure. If the pressure drops either through expansion or due to viscous losses so that PR $<$ 1, term 2 is positive and thus contributes to the overall entropy yield Δs. If the fluid is compressed and PR $>$ 1, term 2 is negative, and the entropy is "removed", i.e. the system gains order. Water vapour, due to its strong intermolecular forces cannot be considered as an ideal gas which poses a difficulty in integrating Eqn. (23). However, considering its small mass fraction at the relevant water injection rates in a compressor (max. 3%), the air and water vapour can be treated together as an ideal gas mixture of approximately the same properties as pure air. In such a case, the entropy production in the gas mixture g with $\dot{m}^g = \dot{m}^a + \dot{m}^v$ is:

$$\dot{S}^g_{gen} = \dot{S}^a_{gen}(1 + w_2 - w_1) \tag{25}$$

A significant portion of entropy "carried" by the vapour is generated due to the phase change as the substance moves from more ordered liquid to gaseous state characterised by higher internal energy and a larger occupied space. The entropy of evaporation is proportional to the heat of evaporation, also referred to as latent heat L, and the temperature T at which the process occurs:

$$s^{ev} = \frac{L}{T} \tag{26}$$

The latent heat is a function of temperature. Therefore, the entropy generation due to evaporation yields:

$$\dot{S}^{v,ev}_{gen} = \dot{m}^a \left[w_2 \frac{L_2}{T^g_{02}} - w_1 \frac{L_1}{T^g_{01}} \right] \tag{27}$$

Note that the entropy yield due to vapour compression and temperature change is already accounted in Eqn. (26). The total entropy generation in a multiphase with air, water, and water vapour yields, therefore:

$$\dot{S}_{gen} = \dot{S}^g_{gen} + \dot{S}^l_{gen} + \dot{S}^{v,e}_{gen} \tag{28}$$

Limitations:

- The approach assumes that at any streamwise position a non-uniform flow parameter (e.g. temperature) can be represented by an equivalent uniform distribution, and therefore by a single mass flow averaged value. In reality, the entropy generation at a given streamwise location will be a sum of the local entropy productions which varies due to the uneven flow field and fluid composition.
- In reality, the droplet temperature is not constant and there will be a small contribution to the entropy generation due to warming up/cooling of liquid.

Compression efficiency

The efficiency of a compressor can be defined as the ratio of isentropic to real work:

$$\eta_c = \frac{w_s^{'}}{w_s} = \frac{h_{02}^{'} - h_{01}}{h_{02} - h_{01}} \tag{29}$$

Subscript s is added to avoid confusion with vapour mass fraction. Using the Gouy-Stoloda theorem for compressors one obtains:

$$h_{02} - h_{02}^{'} = \frac{T_0 \dot{S}_{gen}}{\dot{m}} \tag{30}$$

Combining Eqn. (29) and (30) it can be shown that the wet compressor efficiency for a single-ducted compressor is:

$$\eta_c = 1 - \frac{T_{02}(s_2 - s_1)}{h_{02} - h_{01}} = 1 - \frac{T_{02}\dot{S}_{gen}}{\dot{m}^a (h_{02} - h_{01})} \tag{31}$$

Analogically to the entropy considerations, the change of specific enthalpy in a multiphase flow is (based on $\dot{m}^a$):

$$\begin{aligned} h_2 - h_1 = \\ c^g_p \left[(1 + w_2) T^g_{02} - (1 + w_1) T^g_{01} \right] + c^l_p (f_2 T^l_{02} - f_1 T^l_{01}) \end{aligned} \tag{32}$$

Appendix B: Derivation of Effective Thermal Conductivity

For gases k can be expressed as a function of dynamic viscosity, specific heat at constant volume and a numerical factor f_n which describes the characteristics of the gas molecules:

$$k = f_n \mu c_v \tag{33}$$

Factor f_n can be further approximated to $(9\gamma - 5)/4$ so that the effective thermal conductivity k_{eff} is:

$$k_{eff} = \frac{9\gamma - 5}{4} \mu_{eff} c_v \tag{34}$$